Analysis of air curtain system flow field and droplet drift characteristics of high clearance sprayer based on CFD

Yangyang Song*

(*Jinan Zhiboer Intelligent Technology Co., Ltd., Jinan 250100, China*)

Abstract: High clearance sprayers are widely used in field operations because of their high ground clearance and good passing performance, which can solve the problem of spraying high-stalk crops in the middle and late stages. In this paper, an air curtain system was designed to address the phenomenon of droplet drift in the operation of high clearance sprayers. Based on static pressure recovery theory, the design and optimization of the flow velocity at the outlet of the air curtain were carried out. Using SolidWorks software for modeling, ICEM CFD software to divide meshes, and Fluent software to solve the problem, the air duct model was simulated and drift characteristics of droplets were studied through continuous phase and discrete phase coupling calculation. Using three-factor and three-level orthogonal test, the optimal solution of the model was obtained as follows: a spray pressure of 0.4 MPa, a horizontal wind speed of 2 m/s, a fan frequency of 40 Hz, and a droplet drift rate of 9.38%. According to the degree of influence from large to small, the factors are arranged as follows: horizontal wind speed, fan frequency, and spray pressure. An air curtain system test prototype and a droplet drift rate test platform was built, and flow rate of the air duct outlet and the droplet drift rate were tested under multiple working conditions. Experimental results showed that: when the horizontal wind speed was 2 m/s and 4 m/s, the droplet drift rates were the lowest when frequency was 25 Hz and 35 Hz, respectively, which were 13.65% and 23.88%, respectively. When the horizontal wind speed was 6 m/s and 8 m/s, the droplet drift rates reached the lowest when frequency was 45 Hz, which were 27.02% and 29.78%, respectively. When the horizontal wind speed was 2 m/s, 4 m/s, 6 m/s, and 8 m/s, the droplet drift rates of the optimal auxiliary airflow were reduced by 17.33%, 34.51%, 50.62%, and 67.54%, respectively. Experiments show that the optimal auxiliary air velocity changes when the horizontal wind speed is different.

Keywords: air curtain system, CFD numerical simulation, droplet drift rate, multiple working conditions

DOI: 10.25165/j.ijabe.20241706.8253

Citation: Song Y Y. Analysis of air curtain system flow field and droplet drift characteristics of high clearance sprayer based on CFD. Int J Agric & Biol Eng, 2024; 17(6): 38–45.

1 Introduction

High clearance sprayers are widely used in field spraying due to their high ground clearance and good passing performance. During spraying, external factors such as natural wind may result in uneven spraying and droplet drift. In recent years, many scholars have studied the effects of spraying height, natural wind, and droplet size on droplet drift. Ade et al.[1] compared the air-assisted boom sprayer with the traditional boom sprayer. The results showed that the air-assisted spraying increased the droplet deposition on the back leaves of the potato canopy by 18%, and the loss to the ground was reduced by 37%. A multi-channel air-assisted sprayer developed by Qiu et al.[2] improved the uniformity of droplet coverage by 19.4% compared with the traditional air-assisted sprayer, and the average deposition of droplets in the front, middle, and back of the canopy increased by 32.9% and 50.3%. Salcedo et al.[3] simulated the airflow of a fan and the behavior of spray droplets through the CFD model. The simulation results showed that 44% of the total spray amount reached the target trees, and 28% reached adjacent trees, 20% was deposited on the ground, and 8% was lost to atmospheric drift. Baetens et al.[4] used CFD technology to study the influence of sprayer boom height, natural wind speed, wind direction, and wind curtain wind speed on droplet drift and deposition. The test proved that the model can accurately predict the droplet drift within 5 meters. Khot et al.[5] sprayed citrus trees with different combinations of nozzles and air velocities, and the results showed that 70% air assistance was more effective than 100% air assistance, which blew the spray to the canopy and reduced droplet deposition efficiency. Li et al.[6] proposed two methods for UAV to reduce droplet drift based on CFD and carried out specific simulations to verify their feasibility. Sidahmed et al.[7] designed two symmetrical multi-foil shields, which could effectively reduce the spray drift in the windward and downwind travel directions. Li et al.[8] determined the effects of PWM duty cycle and frequency on spray drift characteristics through wind tunnel experiments. Cooke et al.[9] compared the effects of air-assisted spraying and hydraulic nozzle spraying on droplet drift. The results showed that air-assisted spraying had better penetration to crops than hydraulic spraying. The deposition rate on the backside, the airflow velocity, and the nozzle-to-target spacing had an interactive effect on droplet drift and leaf deposition. Llop et al.[10] studied the application effect of airflow-assisted spray technology in traditional tomato greenhouses and carried out experiments on the deposition amount and droplet distribution uniformity on crops. According to the downwind spray drift curve, Wang et al.[11] fitted the same type of nonlinear equations under four operating conditions of a UAV. Zhao et al.[12] established a droplet deposition model based on bimodal distribution and established a droplet deposition prediction model by using the Monte Carlo method. Sinha et al.[13] quantified the drift of fixed canopy delivery systems and air-assisted sprayers, and results showed that air-assisted spray losses increased, while fixed canopy

Received date: 2023-03-23 **Accepted date:** 2024-11-01

***Corresponding author: Yangyang Song**, ME, research interest: agriculture mechanization. Jinan Zhiboer Intelligent Technology Co., Ltd., Licheng District, Jinan 250100, China. Tel: +86-19861697593, Email: 19861697593@163.com.

delivery systems had minimal air drift losses. Fouque et al.[14] conducted experiments indoors by changing the spray angle through the spray rod and applying the auxiliary effect of air flow, and reached the following conclusions: the increase of auxiliary air flow will make the distribution of droplets more uniform, and changing the spray angle can improve the spray quality to a certain extent. Kira et al.[15] used tree line barriers or buffers to significantly reduce spray drift (up to 50%). Zhang et al.[16] provided the basis for air spray decision-making and droplet deposition prediction by studying the relationship between resistance and wind speed and recorded the changes in frontal area, canopy edge displacement, and optical porosity. Elizabeth et al.[17] used airflow-assisted spray technology to study the uniformity of droplet deposition on artificial plants in a greenhouse. Zhang et al.[18] simulated and analyzed the physical properties of vortex evolution, droplet motion, and evaporation by CFD technology to explain drift and deposition characteristics.

In summary, the research on the influence of airflow assistance on droplet drift has been mainly carried out from the perspectives of airflow velocity, spray angle, spray height, spray pressure, and droplet size. There is a lack of research on the influence of uniformity of the air outlet of the air duct and the interaction of multiple factors on droplet drift. This paper has designed and optimized the wind outlet of the air duct based on the static pressure recovery theory and combined the theory with numerical simulations for studying the interaction of multiple factors on droplet drift.

2 Structural design of air curtain system

According to the anti-drifting principle of an air curtain system for a high ground clearance sprayer, the air duct generates downward auxiliary airflow to force the droplets to move downward to change the movement trajectory of the droplets and reduce the occurrence of droplet drift. The overall structure of an air curtain system for a high ground clearance sprayer is shown in Figure 1.

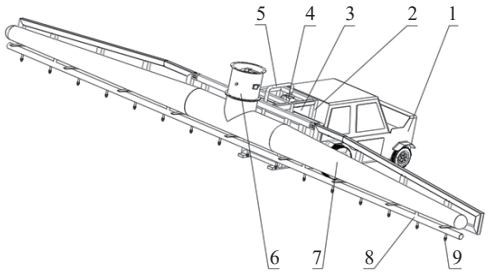

1. Body 2. Frame 3. Pesticide tank 4. Spray pump 5. Outlet hose 6. Axial-flow fan 7. Air duct 8. Spray boom 9. Nozzle

Figure 1 Overall structure of the air curtain system of the ground clearance sprayer

This optimized design was based on the static pressure recovery method. The principle is as follows: changing the downstream cross-sectional area to make the static pressure at the tee of the air duct equal and changing the cross-sectional size makes the air flow rate at the air outlet equal. In a branched pipe, the air flows out of the pipe close to the air outlet so that the air flow rate of the air outlet far away from the pipe decreases in turn, $v_1 > v_2$, as shown in Figure 2. When the total pressure of the fluid remains unchanged, the decrease in wind speed will reduce the dynamic pressure and increase the static pressure, the static pressure of Section 2-2 is greater than the static pressure of Section 1-1, and the calculation method of static pressure recovery is to use the increased static pressure to overcome the resistance of the next pipe to obtain the corresponding cross-sectional area of the pipe and then determine the size of the cross-section.

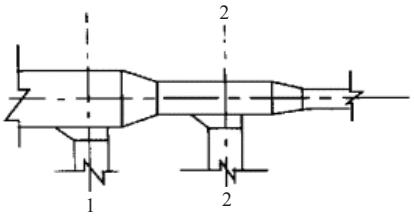

Figure 2 Schematic diagram of static pressure recovery method

The energy equations in the two Sections 1-1 and 2-2 of the duct tee are:

$$z_1 + \frac{\alpha_1 v_1^2}{2g} + \frac{p_1}{\rho g} = z_2 + \frac{\alpha_2 v_2^2}{2g} + \frac{p_2}{\rho g} + h_{1-2} \tag{1}$$

where, z is potential energy; $\frac{v^2}{2g}$ is dynamic pressure energy; $\frac{p}{\rho g}$ is static pressure energy; h is pressure loss.

The calculation method of static pressure recovery needs to meet the following conditions:

$$z_1 = z_2 = 0,\ \ a_1 = a_2 = 1,\ \ h_{1-2} = \varsigma_t \frac{v_2^2}{2g}$$

Equation (1) can be written as

$$\frac{v_1^2}{2g} + \frac{p_1}{\rho g} = \frac{p_2}{\rho g} + (1+\varsigma_t)\frac{v_2^2}{2g} \tag{2}$$

The static pressure recovery value is:

$$\frac{\Delta p}{\rho g} = \frac{p_1}{\rho g} - \frac{p_2}{\rho g} = \frac{v_1^2}{2g} - (1+\varsigma_t)\frac{v_2^2}{2g} \tag{3}$$

Equation (3) can be rewritten as

$$\frac{\Delta p}{\rho g} = K\left(\frac{v_1^2}{2g} - \frac{v_2^2}{2g}\right) \tag{4}$$

where, K is the static pressure recovery coefficient value, taken as 0.75.

To simplify the problem, the following assumptions are made: the flow velocity and static pressure of the section are represented by the average flow velocity of the section and the average static pressure of the section, the flow coefficient and the resistance coefficient along the path are constant, and the air outflow is only due to the static pressure in the pipeline.

The Bernoulli equation is only suitable for the calculation of a single air duct because there is a problem of uneven distribution of air mass in a multi-branched air duct. The air duct was designed as a symmetrical structure, thus, this paper has used a unilateral air duct for calculation and analysis. According to the Bernoulli equation, the following relationship is determined:

$$p_{1-1} - p_{2-2} = \Delta p - K\left(\frac{\rho v_{1-1}^2}{2} - \frac{\rho v_{2-2}^2}{2}\right) \tag{5}$$

where, p_{1-1}, p_{2-2} are static pressure of Sections 1-1 and 2-2, Pa; v_{1-1}, v_{2-2} are wind speed at Sections 1-1 and 2-2, m/s; ρ is density of air, kg/m^3; Δp is total pressure loss between Sections 1-1 and 2-2, Pa.

The formula for calculating the static pressure of Section i:

$$p_i = \frac{\rho v_i^2}{2\mu^2} \tag{6}$$

where, v_i is the velocity of the outlet hole of the i^{th} air duct, m/s; μ is the flow coefficient.

Since the airflow velocity and outlet area of the air duct outlet remain unchanged, $p_{1-1} = p_{2-2}$.

$$\Delta p = K\left(\frac{\rho v_{1-1}^2}{2} - \frac{\rho v_{2-2}^2}{2}\right) \tag{7}$$

Equation (7) can be written as

$$\Delta p = \int_0^{l/n} \frac{\lambda}{D}\frac{\rho v_i^2}{2}\mathrm{d}x \tag{8}$$

where, λ is the drag coefficient along the way; D is the average equivalent diameter of the air duct between Sections 1-1 and 2-2.

If the length of the single air duct l, the outlet hole at the smallest section was set to 1, and so on, as shown in Figure 3; and the entire air volume was sent from the air outlet of the air bag, and the air volume of each air outlet is equal, but:

$$Q_i = \frac{i \times Q_0}{n} \tag{9}$$

where, i is the location of the air duct outlet; Q_i is the air volume at the i^{th} exit; Q_0 is the total air volume of the air curtain inlet section.

$$A_i = \pi\left(\frac{D_i}{2}\right)^2 = \frac{Q_i}{v_i} = \frac{i \times Q_0}{n w_i} \tag{10}$$

where, D_i is the diameter of the section at the outlet of the i^{th} air duct; w_i is the air velocity of the pipe at the cross section i, m/s.

$$D_i = 2\sqrt{\frac{iQ_0}{\pi n w_i}} \tag{11}$$

Since the calculation starts from the end, the average value of D_i and D_{i+1} is approximated to take D_i and we get:

$$K\left(\frac{w_{i+1}^2 - w_i^2}{2}\right) = \frac{\sqrt{\pi}\lambda l w_i^{5/2}}{4\sqrt{inQ_0}} \tag{12}$$

where, λ is 0.02; l is the length of the single air duct.

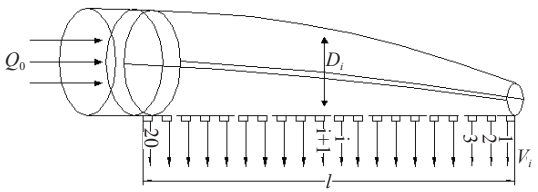

Figure 3 Pipe section

The airflow velocity and aperture of each air outlet of the air duct are equal, $Q_0 = \pi r^2 v n$, where r is the radius of the air outlet, v is the airflow velocity of the air outlet, and n is the number of air outlets. Since it is a single air duct calculation, n is 20. When D_1 is taken as 100 mm, 90 mm, 80 mm, 70 mm, and 60 mm, respectively, the size of the air duct is listed in Table 1.

Analysis of the data shows that the maximum diameter of the air duct is 436.16 mm when D_1 is 100 mm, which is larger than 410 mm and does not meet the design requirements. In other cases, the maximum diameter of the air duct is less than 410 mm, which meets the design requirements. In this study, D_1 was taken as 80 mm, and the maximum equivalent diameter of the air duct was 346.73 mm, which was taken as 350 mm for the convenience of processing.

3 CFD calculation model and flow field analysis

3.1 Diaphragm pump selection

This description takes the variable-section air duct designed based on the static pressure recovery method as an example. A simulation model of a variable cross-section air duct is established with the same size as the model. The model size is listed in Table 2. To reduce the influence of boundary conditions on the flow field simulation, the air duct outlet is 2500 mm long, 600 mm wide, and 1000 mm high. The calculation area is shown in Figure 4. In actual operation in the field, the horizontal natural wind in the opposite direction of the sprayer driving speed has the most serious impact on the spray droplet drift[19], so this study only has considered the horizontal wind speed and ignored wind speed in other directions.

Table 1 Calculation of the equivalent diameter of each section of the air duct (mm)

Air duct section	D_1 diameter				
	100.00	90.00	80.00	70.00	60.00
D_2	140.95	126.81	112.67	98.52	84.38
D_3	172.22	154.90	137.58	120.26	102.94
D_4	198.47	178.47	158.47	138.48	118.48
D_5	221.52	199.16	176.81	154.45	132.09
D_6	242.30	217.81	193.31	168.82	144.33
D_7	261.35	234.90	208.44	181.99	155.53
D_8	279.04	250.76	222.47	194.19	165.91
D_9	295.61	265.61	235.61	205.62	175.62
D_{10}	311.24	279.62	248.00	216.39	184.77
D_{11}	326.08	292.92	259.76	226.60	193.44
D_{12}	340.23	305.59	270.96	236.32	201.69
D_{13}	353.78	317.72	281.67	245.62	209.57
D_{14}	366.78	329.37	291.96	254.55	217.14
D_{15}	379.31	340.58	301.86	263.13	224.41
D_{16}	391.40	351.40	311.41	271.42	231.43
D_{17}	403.10	361.87	320.65	279.42	238.20
D_{18}	414.44	372.02	329.60	287.18	244.76
D_{19}	425.45	381.87	338.28	294.70	251.12
D_{20}	436.16	391.44	346.73	302.02	257.30

Table 2 Geometric model parameters

Inlet diameter/ mm	Maximum diameter of model/mm	Minimum diameter of model/mm	Outlet diameter/ mm	Number of air outlets/ mm	Air outlet spacing/ mm
410	350	80	40	40	50

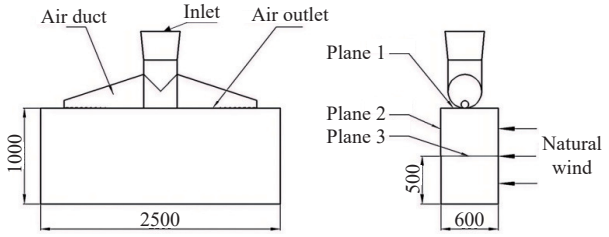

Figure 4 Schematic diagram of variable cross-section air duct

3.2 Model meshing

ICEM CFD software was used to mesh the model. The model has adopted a tetrahedral non-structure, and the two ends of the air duct are densified. The total number of meshes is 1 842 718, and the mesh is shown in Figure 5.

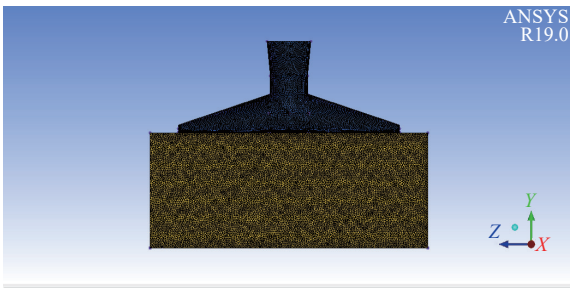

Figure 5 Air duct and calculation area

3.3 Choice of governing equations

For the continuous phase wind fluid simulation, the standard turbulence model is used, and its transport equation is: kinetic energy equation (k-equation):

$$\frac{\partial(pk)}{\partial t}+\frac{\partial(\rho k u_i)}{\partial x_i}=\frac{\partial}{\partial x_j}\left[\left(\mu+\frac{\mu_t}{\sigma_k}\right)\frac{\partial k}{\partial x_j}\right]+G_K+G_b-\rho\varepsilon-Y_M+S_K$$

Dissipation equation (ε-equation):

$$\frac{\partial(\rho\varepsilon)}{\partial_t}+\frac{\partial(\rho\varepsilon u_i)}{\partial x_i}=\frac{\partial}{\partial x_j}\left[\left(\mu+\frac{\mu_t}{\sigma_\varepsilon}\right)\frac{\partial_\varepsilon}{\partial x_j}\right]+C_{1\varepsilon}\frac{\varepsilon}{k}(G_k+C_{3\varepsilon}G_b)-C_{2\varepsilon}\rho\frac{\varepsilon^2}{K}+S_\varepsilon \tag{13}$$

where, ρ is the air density, kg/m^3; ε is the dissipation rate, m^2/s^3; k is the turbulent kinetic energy, m^2/s^2; μ is the continuous phase dynamic viscosity, Pa·s; μ_i is the turbulent viscosity, Pa·s; σ_k is the turbulent dissipation rate Prandtl number; σ_ε is the turbulent kinetic dissipation; t is the time, s; u_i is the speed in the i^{th} direction, m/s; G_K is the generation term of turbulent kinetic energy due to the average velocity gradient, Pa/s; G_b is the generation term of turbulent kinetic energy due to the influence of buoyancy, Pa/s; Y_M is the effect of compressible turbulent pulsation expansion on the total dissipation rate, Pa/s ; S_K is a user-defined item, Pa/s; S_ε is a user-defined item, Pa/s^2; $C_{1\varepsilon}$, $C_{2\varepsilon}$, and $C_{3\varepsilon}$ are empirical constants, which are 1.44, 1.92, and 0.09, respectively. For the discrete phase droplet motion, the Lagrangian method is used to solve the problem, and the transport equation is:

$$\frac{\mathrm{d}u_p}{\mathrm{d}t}=\frac{18\mu C_D Re}{24\rho_p d_{pp}^2\dfrac{g_x(\rho_p-\rho)}{\rho_p}\dfrac{1}{2}\dfrac{p}{p_p}\dfrac{1}{2}\dfrac{\rho}{\rho_p}\dfrac{\mathrm{d}}{\mathrm{d}t_p}} \tag{14}$$

where, u is the continuous phase velocity, m/s; u_p is the particle velocity, m/s; ρ_p is the particle density, kg/m^3; g_x is the acceleration of gravity, m/s^2; Re is the relative Reynolds number; C_D is the drag coefficient.

3.4 Boundary condition settings and CFD simulation algorithm and principle

In this simulation, the effect of gravity was considered. The wind inlet above the air duct model and the horizontal wind speed inlet were set as the velocity inlet boundary, and the outlets were the pressure outlet boundary. The wall was processed with no penetration and no slip boundary conditions.

This paper has adopted the SIMPLE algorithm, first-order upwind style, and second-order upwind style.

3.5 Evaluation index of air duct model

In this paper, the coefficient of variation of the air velocity at the air outlet of the air duct was used as the evaluation index of the air duct model. The coefficient of variation of the air outlet can be calculated by the following equations:

$$\boldsymbol{C}_{v(X)}=\frac{\boldsymbol{S}_{\bar{v}(X)}}{\bar{\boldsymbol{v}}(\boldsymbol{x})}\times 100\% \tag{15}$$

$$\boldsymbol{S}_{\bar{v}(X)}=\sqrt{\frac{\sum(\boldsymbol{v}_i-\bar{\boldsymbol{v}}(\boldsymbol{X}))^2}{\boldsymbol{n}-1}} \tag{16}$$

where, $\boldsymbol{S}_{\bar{v}(X)}$ is the standard deviation of the air velocity at the air outlet.

3.6 Results and analysis of air duct simulation

The air duct flow field was simulated when the fan frequency was 10 Hz, 25 Hz, and 40 Hz (the corresponding theoretical speeds were 560 r/min, 1400 r/min, and 2240 r/min), and the corresponding inlet speeds were 3.46 m/s, 8.66 m/s, and 13.86 m/s. Twenty of the air outlets of the air duct were selected as test ports, starting from the first air outlet on both ends, and every other outlet was used as a test port, as shown in Figure 6, where Figures 6a-6c are the cloud map of the airflow velocity distribution of the variable-section air duct.

The flow field of the equal-section air duct was analyzed, as shown in Figure 7, where Figure 7a is the grid division diagram of the equal-section air bag and the calculation area, and Figures 7b-7d are the fan frequencies of the 10 Hz, 25 Hz, and 40 Hz equal-section air duct airflow velocity distribution cloud maps. Table 3 lists the velocity and variation coefficient of the air duct outlet under different fan frequencies.

After analyzing Table 3, the following conclusions can be drawn:

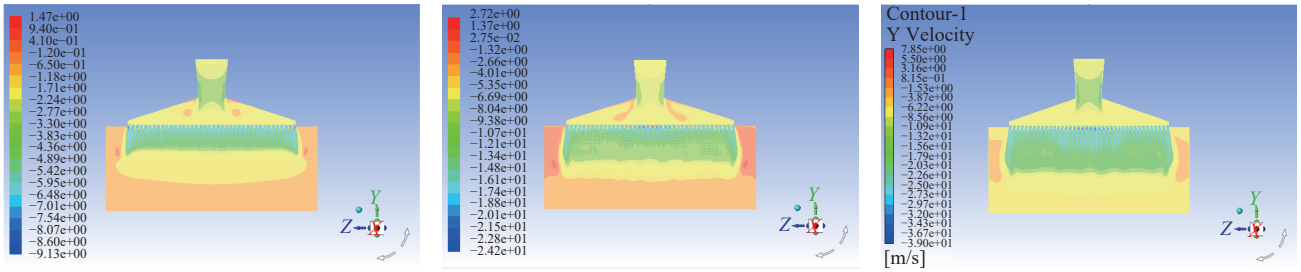

a. Cloud diagram of airflow velocity distribution withvariable cross-section air duct fan frequency at 10 Hz

b. Air flow velocity distribution diagram with variablecross-section air duct fan frequency at 25 Hz

c. Cloud map of airflow velocity distribution withvariable cross-section air duct fan frequency at 40 Hz

Figure 6 Air velocity distribution cloud diagram of variable cross-section air duct

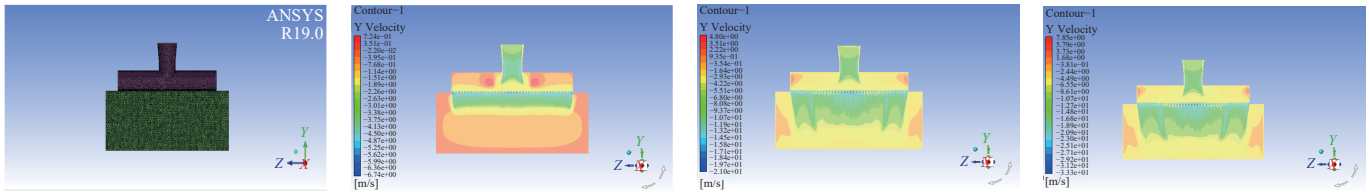

a. Meshing diagram of equal-section air duct and calculation area

b. Contour map of air velocity distribution with equal cross-section air duct fan frequency at 10 Hz

c. Contour diagram of air velocity distribution with equal cross-section air duct fan frequency at 25 Hz

d. Distribution of air flow velocity at a frequency of 40 Hz for a constant-section air duct fan

Figure 7 CFD model of constant cross-section wind

Table 3 Comparison of the speed and the coefficient of variation of each air outlet of the air duct

Fan frequency/ Hz	Average flow velocity of variable section air duct/m·s^{-1}	Average velocity of equal section air duct/m·s^{-1}	Variable section air duct coefficient of variation/%	Equal section air duct coefficient of variation /%	Average velocity difference/ m·s^{-1}	Coefficient of variation difference/%
10	7.83	6.06	4.45	11.50	1.77	5.44
25	19.01	15.63	4.12	6.32	3.38	2.20
40	28.82	23.67	4.66	6.13	5.15	1.47

(1) When the fan frequencies of the variable-section air duct were 10 Hz, 25 Hz, and 40 Hz, the average flow velocities at the outlet were 7.83 m/s, 19.01 m/s, and 28.82 m/s, respectively. The coefficients of variation were 4.45%, 4.12%, and 4.66%. When the fan frequencies of the constant-section air duct were 10 Hz, 25 Hz, and 40 Hz, the average flow velocities at the outlet were 6.06 m/s, 15.63 m/s, and 23.67 m/s. The coefficients of variation were 11.50%, 6.32%, and 6.13%.

(2) When the fan frequency was 40 Hz, the average velocity difference between the variable-section air duct and the constant-section air duct was the largest, at 5.15 m/s; the minimum was 1.77 m/s when the frequency was 10 Hz. The coefficient of variation reached a maximum of 5.44% when the fan frequency was 10 Hz, and it reached a minimum of 1.47% when the frequency was 40 Hz.

4 Analysis of droplet drift characteristics and optimization of parameters under multiple working conditions

4.1 Determination of droplet breakup model and boundary conditions

In this study, the spray source was added and a nozzle was selected to carry it out. According to the atomization mechanism of the nozzle, the flat fan nozzle was selected in Fluent and the TAB model was selected. The motion was set to "trap", which is droplet deposition, and plane 1 and plane 2 were set to "escape" as the particle escape boundary. Considering the effect of gravity, unsteady simulation was adopted. The simulation time was 5 s, the iteration step was 0.05 s, and the number of time steps was 100.

4.2 Evaluation index of droplet drift rate

This paper has ignored the natural wind component in the direction of the air duct, and the movement of water droplets in the direction of the air duct was not considered. Therefore, the number of particles passing through face 1 and face 2 were counted as the number of drifting droplets, and the number of particles passing through plane 3 were counted as the number of particles deposited by the droplet.

The droplet drift rate is defined as:

$$\eta = \frac{m_1}{m_1 + m_2} \times 100\% \tag{17}$$

where, $m_1 = \sum_{i=1}^{N_1} \frac{4}{3}\rho\pi r_i^3 n_i$, $m_2 = \sum_{i=1}^{N_2} \frac{4}{3}\rho\pi r_i^3 n_i$; m_1 is drifted particle mass; m_2 is deposited particle mass; N_1 is the number of particles drifting through plane 1 and 2 in Figure 4; ρ is droplet density; n_i is the number of particles in i^{th} particles; r_i is particle radius in i^{th} particles; N_2 is the number of particles passing through plane 3 in Figure 4.

Figure 8 shows the particle distribution trajectories of the droplets in the natural spray state and the particle distribution trajectory diagram of the horizontal wind speed.

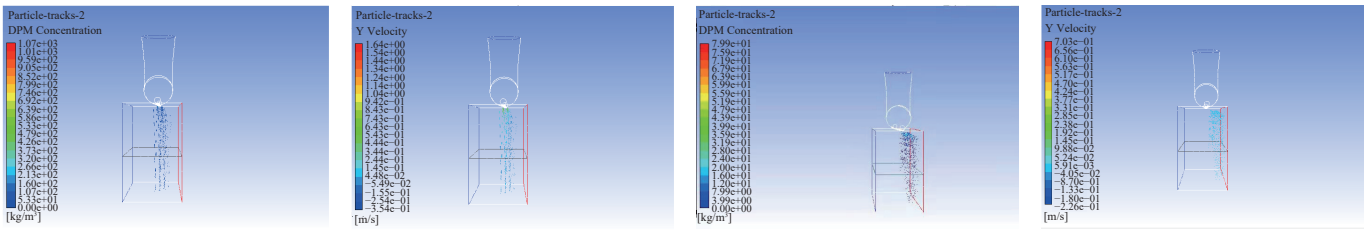

a. Particles distribution trajectory of naturally falling droplets

b. Cloud map of particles velocity distribution in naturally falling fog droplets falling droplets

c. Droplet particles distribution trajectory with horizontal wind speed

d. Cloud map of droplet particles velocity distribution with horizontal wind speed

Figure 8 Droplet tracking trajectory diagram and velocity distribution cloud diagram

4.3 Analysis of numerical simulation results of droplet drift under multiple working conditions

Design-expert8.0 software was used to analyze the results of the orthogonal test, and the spray pressure, horizontal wind speed, and fan frequency were chosen as variables. The test factors and levels are listed in Table 4.

Table 4 Test factor level coding table

Coding level	Spray pressure/ MPa	Horizontal wind speed/m·s^{-1}	Fan frequency/ Hz
–1	0.2	2	10
0	0.4	4	25
1	0.6	6	40

This test was a three-factor and three-level orthogonal test at a nozzle height of 500 mm. The test results are listed in Table 5 and Table 6.

According to the data in Table 6, the above results were imported into the data analysis software, and the Quadratic model was selected to obtain the quadratic regression equation between the droplet drift rate and each factor:

$$y = 31.85 + 1.03A + 15.71B - 11.19C + 0.78AB - 0.38AC - 5.34BC - 2.54A^2 - 3.05B^2 + 2.13C^2 \tag{18}$$

where, y is the droplet drift rate; A is the spray pressure; B is the horizontal wind speed; and C is the fan frequency. It can be seen from the variance analysis results of the regression model in Table 6 that the p-value of the regression model was less than 0.0001, indicating that the regression model was highly significant. Additionally, the p-value of the model's lack of fit was 0.7920, which is greater than 0.05, indicating that the model's lack of fit was not significant. The fitting degree of the model was relatively high. From the p-values of spray pressure, horizontal wind speed, and fan frequency, it can be judged that the three experimental factors had a significant impact on the droplet drift rate. Among

Table 5 Orthogonal test results

Test No.	Spray pressure A /MPa	Horizontal wind speed B /m·s^{-1}	Fan frequency C /Hz	Droplet drift rate/%
1	0.60	4.00	40.00	20.65
2	0.40	4.00	25.00	31.28
3	0.40	6.00	10.00	63.16
4	0.40	2.00	10.00	21.07
5	0.60	2.00	25.00	11.05
6	0.40	6.00	40.00	30.11
7	0.40	4.00	25.00	31.02
8	0.20	4.00	40.00	19.85
9	0.40	2.00	40.00	9.38
10	0.40	4.00	25.00	31.92
11	0.20	4.00	10.00	41.47
12	0.60	6.00	25.00	44.03
13	0.60	4.00	10.00	43.79
14	0.20	6.00	25.00	39.89
15	0.40	4.00	25.00	32.68
16	0.20	2.00	25.00	10.04
17	0.40	4.00	25.00	32.35

them, the horizontal wind speed and fan frequency had extremely significant effects on the droplet drift, while the spray pressure had a significant effect. The factors of influence from large to small were: horizontal wind speed, fan frequency, and spray pressure. The fitted regression model had a high degree of accuracy and reliability due to the coefficient of variation of 1.97%, and the correlation between the predicted value of the droplet drift rate and the experimental value was a straight line (as shown in Figure 9). According to the analysis results of the regression model, Design-Expert8.0 software was used to draw the 3D response plane of the interaction of various factors for the droplet drift rate.

Figures 10a-10c are response planes of the interaction between fan frequency and spray pressure, the response surfaces of the interaction between fan frequency and horizontal wind speed, and response surfaces of interaction between horizontal wind speed and

Table 6 Variance analysis of the quadratic regression model of droplet drift rate

Source of variance	Mean square	Degree of freedom	Sum of square	*p*-value
Model	318 463	9	353.85	<0.0001
A	8.55	1	8.55	0.0017
B	1973.49	1	1973.49	<0.0001
C	1001.26	1	1001.26	<0.0001
AB	2.45	1	2.45	0.0338
AC	0.58	1	0.58	0.2418
BC	114.06	1	114.06	<0.0001
A^2	27.24	1	27.24	<0.0001
B^2	39.26	1	39.26	<0.0001
C^2	19.17	1	19.17	0.0002
residual	2.47	7	0.35	
lack of fit	0.52	3	0.17	0.7920
pure error	1.96	4	0.49	
sum	3187.10	16		

spray pressure. The optimal solution of the model was a droplet drift rate of 9.38% under a spray pressure of 0.4 MPa, horizontal wind speed of 2 m/s, and fan frequency of 40 Hz.

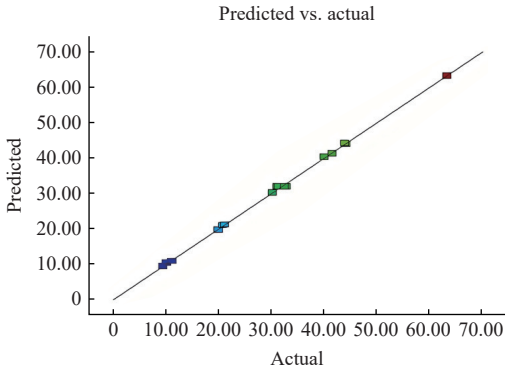

Figure 9 Correlation between the predicted value of droplet drift rate and the experimental value

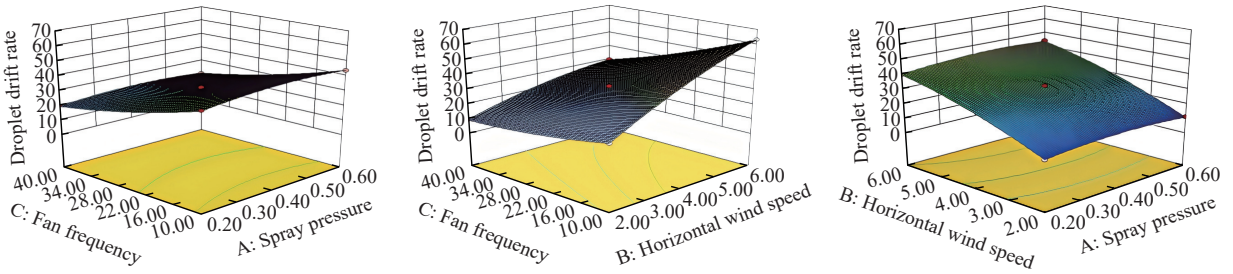

a. Fan frequency and spray pressure interaction response surface

b. Fan frequency and horizontal wind speed interaction response surface

c. Response surface of the interaction between horizontal wind speed and spray pressure

Figure 10 The influence of multi-factor interaction on droplet drift

5 Prototype construction and testing

The air curtain system test system was mainly composed of a frame, an axial flow fan, an air curtain air duct, a frequency converter, a spray system, and a droplet collection container. There was no leakage, the speed of the axial flow fan was controlled by the frequency converter, the air duct was made of canvas, the minimum diameter of both ends of the air duct was 80 mm, and the maximum diameter was 350 mm. The spray system was composed of spray boom, nozzles, hose, pressure gauge, spray pump, and pesticide tank. The spray pressure was adjusted by adjusting the pressure-regulating screw on the spray pump. The main parameters of the test device are listed in Table7.

Table 7 Main parameters of the test device for air curtain system of the high ground clearance sprayer

Device	Technical parameter	Value
XTL diaphragm pump	Flow/L·min^{-1}	4
Electronic balance	Weighing range/g	0.5-3000
Y-100 pressure gauge	Measuring range/MPa	0-0.6
German Lechler ST110-01 nozzle	Atomization angle/(°)	110
GM816 Anemometer	Measuring range/m·s^{-1}	0.1-30
SF3.5-2 axial flow fan	Maximum air volume/m^3·h^{-1}	6000
Inverter Delta VFD-M	Power/kW	0.75

The test site was sealed to avoid external interference. The nozzle was 500 mm away from the collection surface of the droplet collection container, and the horizontal distance between the nozzle and the edge of the inner side of the droplet collection container was 300 mm. In this test, the influence of the running speed of the sprayer and the horizontal natural wind speed in the opposite direction were comprehensively considered, and the horizontal wind speed was simulated by the axial flow fan. The test site is shown in Figure 11.

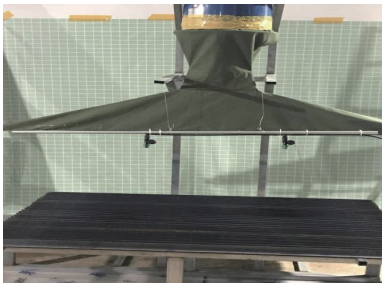

Figure 11 Test site of droplet drift rate test

5.1 Experiment of measuring the flow velocity at the air outlet of the air curtain

The GM816 anemometer was used to measure the speed of the wind outlet. The anemometer was placed close to the outlet of the air duct, the measuring position was kept still until the displayed number on the anemometer was stable for approximately three seconds, and the wind speed value for each orifice at different fan speeds was read. The average value of three measurements was taken. The test points were consistent with the numerical simulation test points.

As can be seen in Table 8, when the fan frequency was 10 Hz, 25 Hz, and 40 Hz, the average airflow velocity value of the actual air duct outlet was smaller than the average value of the numerical simulation. The maximum difference value was 1.72 m/s when the fan frequency was 40 Hz, and the minimum was 0.73 m/s when the fan frequency was 10 Hz. The variation coefficient of the air duct outlet was at a maximum of 0.99 when the fan frequency was 10 Hz, and the minimum was 0.02 when the fan frequency was 25 Hz. There were few differences between the numerical simulation and the experimental data.

Table 8 Comparison of air velocity and coefficient of variation between numerical simulation and experiment

Fan frequency/ Hz	Numerical simulation of the mean air velocity at the air outlet of the air duct/m·s^{-1}	Average air velocity at the air outlet of the test air duct/m·s^{-1}	Numerical simulation coefficient of variation/ %	Test coefficient of variation/ %	Air velocity difference at air duct outlet/m·s^{-1}	Coefficient of variation difference/ %
10	7.83	7.10	4.45	3.46	0.73	0.99
25	19.01	17.90	4.12	4.10	1.11	0.02
40	28.82	27.10	4.66	4.34	1.72	0.32

5.2 Multi-condition droplet drift rate test of air curtain system

In this study, the spray pressure was kept steady at 0.5 MPa, which is commonly used in the operation. The fan frequency was set to 0 Hz, 15 Hz, 25 Hz, 35 Hz, and 45 Hz, and droplet drift rate was tested at horizontal wind speeds of 2 m/s, 4 m/s, 6 m/s, and 8 m/s. In actual experiments, it is difficult to count the droplet particles, so the mass of droplets deposited on each surface in the experiment is taken as the calculation result of droplet drift. The droplet drift rate was used as the evaluation index of droplet drift, and the ratio of the droplet drift amount to the total mass of the droplet spray was defined as the droplet drift rate to reflect the influence of various factors on the droplet drift.

$$D_f = \frac{Q-D}{D} \times 100\% \quad (19)$$

where, D_f is droplet drift rate, %; Q is the total mass of spray droplets, g; and D is spray droplet deposition, g.

The weighing instrument used in this test was an electronic balance, with specifications MAX=3000 g, e=0.1 g, d=0.01 g. The pressure of the water pump was adjusted by adjusting its pressure-regulating screw, and the spray mass of the measured spray in the natural state was 1587.4 g. The test results of droplet drift rate are listed in Table 9.

The following conclusions can be drawn from Table 9:

(1) The predicted results were close to the test results when the fan frequency was 0 Hz. The optimal fan frequency was different from the test when the horizontal wind speeds were 2 m/s and 4 m/s, and it was consistent with the test when the wind speeds were 6 m/s and 8 m/s.

(2) The optimal fan frequency in the test was 25 Hz when the horizontal wind speed was 2 m/s, and the lowest value of the droplet drift rate was 13.65%, lower than 30.98% with the fan frequency of 0 Hz. The droplet drift rate increased when the fan frequencies were 35 Hz and 45 Hz.

(3) The optimal fan frequency in the test was 35 Hz when the horizontal wind speed was 4 m/s, and the droplet drift rate was 23.88%, lower than 58.39% with the fan frequency of 0 Hz.

(4) The optimal fan frequency in the test was 45 Hz when the horizontal wind speeds were 6 m/s and 8 m/s, and the droplet drift rates were 27.02% and 29.78%, respectively, lower than 77.64% with the fan frequency of 0 Hz.

Table 9 The droplet drift rate corresponding to each working condition when the spray pressure is 0.5 MPa

Horizontal wind speed/m·s^{-1}	Fan frequency/ Hz	CFD prediction of droplet drift rate/%	Test droplet drift rate /%
2	0	28.57	30.98
2	15	17.55	19.26
2	25	12.58	13.65
2	35	9.50	14.37
2	45	8.32	16.98
4	0	56.62	58.39
4	15	40.26	43.65
4	25	31.73	34.77
4	35	25.09	23.88
4	45	20.35	24.59
6	0	78.56	77.64
6	15	56.87	60.49
6	25	44.77	47.78
6	35	34.58	35.95
6	45	26.27	27.02
8	0	94.40	97.32
8	15	67.36	79.49
8	25	51.71	55.03
8	35	37.95	40.96
8	45	26.09	29.78

6 Conclusions

This paper has drawn the following conclusions through theoretical calculations and prototype tests:

(1) The difference between the constant-section air duct and the variable-section air duct was compared through CFD numerical simulation. When the fan frequency was 40 Hz, the average velocity difference between the two air ducts was the largest, at 5.15 m/s, and the difference was the smallest when the frequency was 10 Hz, at 1.77 m/s. The coefficient of variation had a maximum difference of 5.44% when frequency was 10 Hz and a minimum difference of 1.47% when frequency was 40 Hz. Air flow rate at the air outlet was higher and more uniform, with a lower coefficient of variation.

(2) The CFD prediction model and 17 sets of orthogonal experiments were established through discrete phase and continuous phase coupling calculations. According to the degree of influence from large to small, the factors are arranged as follows: horizontal wind speed, fan frequency, spray pressure. The optimal solution of the model is a spray pressure of 0.4 MPa, a horizontal wind speed of 2 m/s, and a fan frequency of 40 Hz, resulting in a droplet drift rate of 9.38%.

(3) A prototype of the air curtain system and the test platform were built for the droplet drift rate test. When fan frequency was 10 Hz, 25 Hz, and 40 Hz, respectively, the average airflow velocity value of the actual air duct outlet was smaller than the average value of the numerical simulation. The maximum wind speed was 1.72 m/s when the frequency was 40 Hz, and the minimum wind speed was 0.73 m/s when the frequency was 10 Hz. The coefficient of variation of the air duct outlet had a maximum value of 0.99 when the frequency was 10 Hz, and a minimum value of 0.02 when the frequency was 25 Hz.

(4) The droplet drift rate was tested under multiple working conditions when the spray pressure was kept steady at 0.5 MPa. When horizontal wind speeds were 2 m/s and 4 m/s, the drift rates were the lowest when frequencies were 25 Hz and 35 Hz, respectively, at 13.65% and 23.88%, respectively. When the horizontal wind speeds were 6 m/s and 8 m/s, the droplet drift rates reached their lowest when frequency was 45 Hz, at 27.02% and 29.78%, respectively. When the horizontal wind speeds were 2 m/s, 4 m/s, 6 m/s, and 8 m/s, the droplet drift rates of the optimal auxiliary airflow were reduced by 17.33%, 34.51%, 50.62%, and 67.54%, respectively. The fit was higher at horizontal wind speeds compared with the unassisted airflow.

[References]

[1] Ade G, Rondelli V. Performance of an air-assisted boom sprayer in the control of Colorado beetle infestation in potato crops. Biosystems Engineering, 2007; 97(2): 181–187.

[2] Qiu W, Li X L, Li C C, Ding W M, Lv X L, Liu Y D. Design and test of a novel crawler-type multi-channel air-assisted orchard sprayer. Int J Agric & Biol Eng, 2020; 13(6): 60–67.

[3] Salcedo, R, Vallet A, Granell R, Garcerá C, Moltó E, Chueca P. Eulerian–Lagrangian model of the behaviour of droplets produced by an air-assisted sprayer in a citrus orchard. Biosystems Engineering, 2017; 154: 76–91.

[4] Baetens K, Nuyttens D, Verboven P, De Schampheleire M, Nicolai B, Ramon H. Predicting drift from field spraying by means of 3D computational fluid dynamics model. Computers and Electronics in Agriculture, 2007; 56(2): 161–173.

[5] Khot L R, Ehsani R, Albrigo G, Larbi P A, Landers A, Campoy J, et al. Air-assisted sprayer adapted for precision horticulture: Spray patterns and deposition assessments in small-sized citrus canopies. Biosystems Engineering, 2012; 113(1): 76–85.

[6] Li H Z, Zhu H, Jiang Z H, Lan Y B. Performance characterization on downwash flow and spray drift of multirotor unmanned agricultural aircraft system based on CFD. Int J Agric & Biol Eng, 2022; 15(3): 1–8.

[7] Sidahmed M M, Awadalla H H, Haidar M A. Symmetrical multi-foil shields for reducing spray drift. Biosystems Engineering, 2004; 88(3): 305–312.

[8] Li L L, Chen L P, Zhang R R, Tang Q, Yi T C, Liu B Q, et al. Spray drift characteristics of pulse-width modulation sprays in wind tunnel. Int J Agric & Biol Eng, 2022; 15(4): 7–15.

[9] Cooke B K, Hislop E C, Herrington P J, Western N M, Humpherson-Jones F. Assisted spraying of arable crops, in relation to deposition, drift and pesticide performance. Crop Protection, 1990; 9(4): 303–311.

[10] Llop J, Gil E, Gallart M, Contador F, Ercilla M. Spray distribution evaluation of different settings of a hand-held-trolley sprayer used in greenhouse tomato crops. Pest Management Science, 2015; 72(3): 505–516.

[11] Wang J, Lan Y B, Zhang H H, Zhang Y L, Wen S, Yao W X, et al. Drift and deposition of pesticide applied by UAV on pineapple plants under different meteorological conditions. Int J Agric & Biol Eng, 2018; 11(6): 5–12.

[12] Zhao L. Research on air curtain system optimization and intelligent control strategy based on bimodal distribution drift deposition model. Shandong Agricultural University, 2020. DOI: 10.27277/d.cnki.gsdnu.2020.000935.

[13] Sinha R, Ranjan R, Khot L R, Hoheisel G A, Grieshop M J. Drift potential from a solid set canopy delivery system and an axial–fan air–assisted sprayer during applications in grapevines. Biosystems Engineering, 2019; 188: 207–216.

[14] Foque D, Pieters J G, Nuyttens D. Spray deposition and distribution in abay laurel crop as affected by nozzle type, air assistance and spray direction when using vertical spray booms. Crop Protection, 2012; 41: 77–87.

[15] Kira O, Dubowski Y, Linker R. In-situ open path FTIR measurements of the vertical profile of spray drift from air-assisted sprayers. Biosystems Engineering, 2018; 139: 32–41.

[16] Zhang C, Zhou H, Xu L, Ru Y, Ju H, Chen Q. Wind tunnel study of the changes in drag and morphology of three fruit tree species during air-assisted spraying. Biosystems Engineering, 2022; 218: 003.

[17] Musiu E M, Qi L, Wu Y. Spray deposition and distribution on the targets and losses to the ground as affected by application volume rate, airflow rate and target position. Crop Protection, 2019; 116: 170–180.

[18] Zhang B, Tang Q, Chen L P, Zhang R R, Xu M. Numerical simulation of spray drift and deposition from a crop spraying aircraft using a CFD approach. Biosystems Engineering, 2017; 166: 184–199.

[19] Yuan J, Liu X M, Zhang X H, Zuo W L, Wang X, Chen L P. Modeling and compensation for characteristic of droplet drift on air-assisted boom spraying accounting for wind speeds. Transactions of the CSAE, 2013; 29(14): 45–52.